Superparamagnetic Iron Oxide–Enhanced Magnetic Resonance Imaging of Neuroinflammation in a Rat Model of Radicular Pain

Daniel L.J. Thorek, Christine L. Weisshaar, Julie C. Czupryna, Beth A. Winkelstein, and Andrew Tsourkas

Abstract

In many clinical cases of radicular pain, no noticeable neuropathology is detected by conventional medical imaging strategies. Superparamagnetic iron oxide (SPIO) nanoparticles were evaluated as magnetic resonance contrast agents to specifically detect neuroinflammation at sites of painful injury in a rat model of cervical nerve root compression. Two separate groups of rats were used: an injury group that underwent controlled transient compression of the dorsal root and a sham group that received the same surgical procedures but no injury. Precontrast magnetic resonance imaging (MRI) was performed 6 days after surgery, followed by administration of SPIO via tail vein injection. After 24 hours, T_2*-weighted imaging at the site of root injury revealed a postcontrast enhancement of 72.9 $\pm$ 31%. This was significantly greater than that of injured animals prior to SPIO administration (5.3 $\pm$ 12.9%). SPIO did not generate any significant postcontrast enhancement in the nerve roots of the sham group. Histology confirmed colocalization of SPIO with macrophage at the injury site. These findings suggest that SPIO-enhanced MRI may be a valuable tool to identify otherwise undetectable nerve root compression and enable improved patient management.

CERVICAL RADICULOPATHY is a neurologic condition characterized by symptoms of pain or dysfunction originating from a cervical spinal nerve or nerve roots. This condition is often severely debilitating and manifests as hypersensitivity to mechanical and temperature stimuli in the neck and radiating in to the arm.[1,2] For some, pain persists for several years after injury, leading to chronic disability,[3] with staggering societal and economic costs,[4,5] and affects as many as 71% of adults.[6,7]

Radicular pain commonly results from mechanical and/or chemical insult of the nerve roots.[8–10] Radiologic evidence of neural impingement, such as disk collapse and/or protrusion, spondylosis, or foraminal occlusion, is seen in as many as 44% of lower back pain[11] and 68% of neck pain cases.[3] However, in most of the remaining cases, no noticeable tissue compression or pathology is detected.

Consequently, pain may result from a transient mechanical injury that is not apparent through conventional diagnostic radiology but nonetheless produces significant neuronal damage.[12] The challenge of diagnosing this clinical syndrome is exacerbated by the high rates of positive radiologic findings in asymptomatic subjects.[13–16]

Recent studies have reported that local inflammation can be induced by transient mechanical injuries to neural tissues.[8,17] In a rat model of cervical radiculopathy, transient compression of the C7 cervical dorsal nerve root produces persistent behavioral sensitivity, as measured by mechanical allodynia (sensitivity to an otherwise nonpainful mechanical stimulus).[18–20] Transient compression is also sufficient to produce wallerian degeneration, along with hallmarks of neuroinflammation, including increased upregulation and expression of neuropeptides, growth factors, and cytokines, and sustained inflammatory cell activation at the injury site and in the spinal cord.[17,21,22] Infiltrating macrophages ingest axonal debris at the injury site and have been shown to be a principal element in the development of pain.[23–25]

It has been previously demonstrated that superparamagnetic iron oxide (SPIO) can be used to detect macrophage in vivo. Following their phagocytic uptake, these nanometer-sized contrast agents generate local hypointensity in T_2- and T_2*-weighted images. SPIO has

From the Department of Bioengineering, University of Pennsylvania, Philadelphia, PA.

Address reprint requests to: Andrew Tsourkas, PhD, Department of Bioengineering, University of Pennsylvania, 210 S. 33rd Street, Room 240 Skirkanich Hall, Philadelphia, PA 19104; e-mail: atsourk@seas. upenn.edu.

been used to study the inflammatory processes of a number of pathologies, including soft tissue infection,[26–28] implant rejection,[29] and atherosclerosis,[30–32] among others.[33] Previous neuroinflammatory imaging applications of SPIO include multiple sclerosis,[34–37] peripheral nerve injury,[38,39] and cell migration in severe spinal cord trauma.[40,41] However, there are no in vivo cellular imaging studies investigating the use of SPIO to identify and/or localize the anatomic site of pain resulting from a controlled, transient neural injury.

The purpose of this study was to evaluate SPIO detection of a cellular inflammatory response following transient nerve root compression sufficient to produce sustained behavioral sensitivity. Application of SPIO to investigate neural damage in vivo may provide a powerful tool for both the diagnosis and assessment of therapy of this otherwise occult neuropathy.

Materials and Methods

Materials

All chemicals and equipment were purchased from Fisher Scientific (Pittsburgh, PA), unless otherwise noted.

Animal Care and Use

Male Holtzman rats (Harlan Sprague-Dawley, Indianapolis, ID) were housed under US Department of Agriculture– and Association for Assessment an Accreditation of Laboratory Animal Care–approved conditions with free access to food and water. All experimental procedures were approved by the University of Pennsylvania Institutional Animal Care and Use Committee and carried out under the guidelines of the Committee for Research and Ethical Issues of the International Association for the Study of Pain.[42]

Nanoparticle Synthesis and Characterization

SPIO nanoparticles were prepared using the chemical coprecipitation technique.[43] Briefly, a solution of iron salts, 1.97 g of $FeCl_3$ and 0.7313 g of $FeCl_2$ (each in 12.5 mL of dH_2O), was dissolved in the presence of 25 g dextran-T10 (GE Healthcare, Waukesha, WI) in 50 mL dH_2O under nitrogen gas. The vessel was cooled to 4°C, and 15 mL of ammonium hydroxide was added. This solution was then heated to 90°C for 1 hour, cooled overnight, and then purified from aggregates by ultracentrifugation at 20k RCF. The supernatant containing nanoparticles was diafiltered against greater than 20 volumes of 0.02 M citrate, 0.15 M sodium chloride buffer, using a 100 kDa cutoff membrane (GE Healthcare). Finally, particles were exchanged into pH 7.4 phosphate-buffered saline (PBS), 0.2 μm syringe filtered, and stored at 4°C.

SPIO nanoparticles were characterized by dynamic light scattering to determine hydrodynamic diameter using a Zetasizer Nano-S (Malvern Instruments, Malvern, UK). The transverse relaxivity, R_2, of the particles was calculated as the slope of $1/T_2$ against iron concentration. T_2 relaxation times were determined using a Bruker mq60 MR relaxometer (Bruker, Milton, ON) operating at 1.41 T (40°C) using a standard Carr-Purcell-Meiboom-Gill muli-techo sequence ($\tau = 1.5$ ms and 2 dummy echoes).

Surgical Procedures

The transient unilateral nerve root compression injury has been previously described and reliably induces sustained behavioral sensitivity that lasts for nearly 3 weeks.[44–47] Briefly, a hemilaminectomy and a facetectomy were performed at the C6–C7 level of the right side to expose the C7 roots. For painful injury, a microvascular compression clip (World Precision Instruments, Inc., Sarasota, FL) was used to apply a 10 gmf compression to the dorsal nerve root for 15 minutes ($n = 6$; Figure 1A). Identical surgical procedures were carried out for the sham group except that the nerve root was exposed only, without any compression ($n = 4$). The surgery site was sutured and closed with surgical staples. Surgical procedures were performed under inhalation anesthesia using 4% isoflurane for induction and 2% for maintenance. At the time of surgery (day 0; Figure 1B), all rats weighed between 275 and 308 g. Rats were continuously monitored following recovery.

Magnetic Resonance Imaging

All experiments were performed using a 9.4 T horizontal small-animal Varian Magnetic Resonance Imaging System equipped with a 25 g/cm gradient insert (Varian, Palo Alto, CA) at the Small Animal Imaging Facility in the Department of Radiology at the University of Pennsylvania. Imaging was performed using a dual-coil system; a 7 cm diameter volume coil was actively detuned for use with a 2.5 cm loop receive-only surface coil (InsightMRI, Worcester, MA).

Rats were anesthetized prior to imaging, as described above, and placed supine into a custom-built stereotactic restraint device that held the surface coil to the cervical
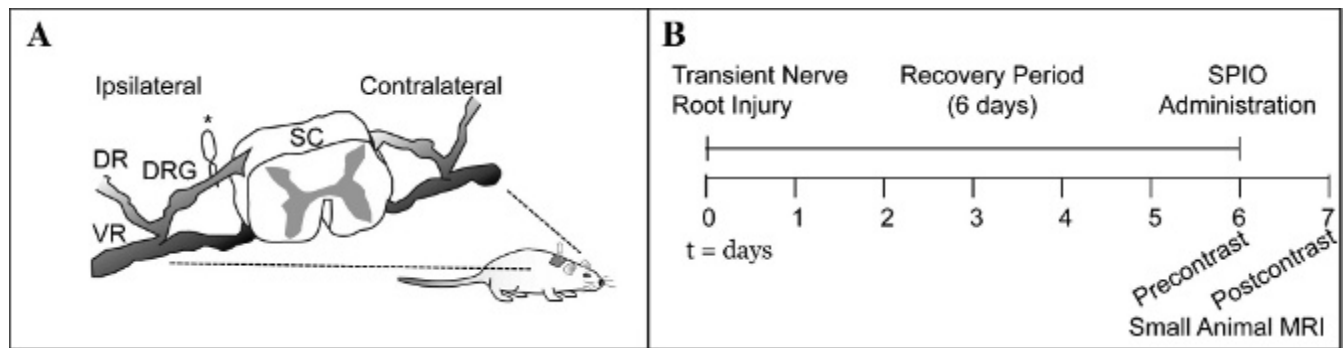
Figure 1. Schematic of transient nerve root compression injury and imaging timeline. *A,* The painful injury is provoked by transient compression of the right C7 dorsal nerve root. A hemostatic compression clip (*) is applied proximal to the dorsal root ganglion (DRG) following the disclosure of the nerve root. The ventral ramus (VR) and dorsal ramus (DR) are also indicated. SC = spinal cord. *B,* The timeline for the experiment shows that following 6 days of recovery, precontrast images of the animals are acquired with a 9.4 T MR. SPIO nanoparticles are tail vein injected following the precontrast imaging session, and postcontrast scanning is performed 24 hours later. MRI = magnetic resonance imaging.

spine. A coaxial breathing apparatus delivered anesthetic throughout the scan and removed CO_2 and excess isoflurane. Temperature and electrocardiography probes were used to monitor the rats in the 37°C environment supplied by an air heating system (SA Instruments, Inc., Stony Brook, NY).

Precontrast image sets were acquired at day 6 following surgery (see Figure 1B). After the precontrast imaging session, 10 mg Fe/kg (approximately 300 μL) was delivered systemically by tail vein injection. Postcontrast image sets were acquired 24 hours later, on day 7 following surgery (see Figure 1B). Identical imaging procedures were used for both of the pre- and postcontrast imaging sessions. In vivo magnetic resonance imaging (MRI) of the C6 and C7 spinal cord and nerve roots was performed using *VnmrJ* software (Varian). The MRI protocol began with several low-resolution, that is, "scout," sequences to locate the C6 and C7 nerve roots. This was followed by a T_2*-weighted gradient echo multislice sequence (repetition time 200 ms, echo time 5.5 ms, 20° flip angle) in the axial plane. Greater T_2*-weighting, although desired, was precluded owing to the proximity (and enclosure) of interrogated anatomy to bone. Fifteen interleaved slices were typically acquired, with a thickness of 0.5 mm, number of excitations = 8, number of readout points = 256, number of phase encoding steps = 256, and a field of view of 5 cm × 5 cm.

Image and Statistical Analyses

Image sets were analyzed using *ImageJ* (National Institutes of Health, Bethesda, MD) following their conversion using the Multi FDF Opener plug-in (Shanrong Zhang, University of Texas Southwestern Medical Center, Dallas, TX). User-defined regions of interest (ROI) of equal area

were set for the ipsilateral and contralateral (control) C6 and C7 nerve roots, as well as two background (paraspinal muscle) locations, under radiologist-blinded (pre-, post-contrast, injured, or sham) conditions.

On a slice-specific basis, the relative signal intensity (rSI) was calculated by division of the mean intensity of the ROI at each nerve root by that of the paraspinal muscle. For each subject, this value was then normalized to the rSI maxima of the C6 nerve root to give the normalized rSI (nrSI) for ipsilateral and contralateral roots. Quantitative comparison of the pre- and postcontrast C7 nerve roots, as well as between injured and sham groups, was made possible by then computing the average difference of the normalized rSI peak and immediately adjacent slices.

MRI findings, the presence or absence of enhancement, were considered significant if $p < .01$. A two-tailed Mann-Whitney test was used.

Tissue Harvest and Immunohistochemical Staining

Tissue was harvested from all rats immediately following the final imaging session on day 7 (see Figure 1B). Transcardiac perfusion was performed using PBS and then a 4% paraformaldehyde-in-PBS mixture; the cervical spinal cord was exposed and the C7 level was bisected to enable removal of the nerve roots and spinal cord en bloc on each of the ipsilateral and contralateral sides separately. Tissue samples were embedded in paraffin to enable axial sectioning (10 μm thick). Nanoparticles were localized in the tissue by Prussian blue staining for iron oxide using a 1:1 mixture of 2% potassium ferrocyanide and 2% HCl for 20 minutes. Sections were rinsed in dH_2O, dehydrated, cleared in Citrisolv, and then coverslipped using Permount. Serial sections were also immunostained to

colocalize macrophages with SPIO; activated macrophages were stained using an antibody against the CD68 receptor (ED-1, Serotec, Oxford, UK). A horse antimouse secondary antibody (Vector, Burlingame, CA) was used and developed using the ABC kit (Vector). Sections were dehydrated, cleared, and then mounted.

Results

Precontrast images were acquired after 6 days of recovery from surgery. Dextran-coated SPIO nanoparticles, with a 29 nm hydrodynamic diameter and a relaxivity (R_2) of approximately 104 $mM^{-1}s^{-1}$, were then injected at a dose of 10 mg Fe/kg. The following day, imaging was repeated. The cervical nerve roots at the C6 and C7 nerve root levels were visualized with 0.5 mm thin axial slices in series using a T_2*-weighted multislice gradient echo sequence.

A representative axial acquisition from each group, pre- and postcontrast, is shown in Figure 2. Scans of the rat cervical spine show the spinal cord at the center surrounded by vertebral bone enclosed in muscle. Careful axial slice selection afforded visualization of both the ipsilateral and contralateral roots in the field of view, allowing for an inherent control (contralateral root) to be included throughout imaging. Bilateral roots can be readily seen in the precontrast images for both the injured and sham groups; however, there is a clear loss of signal in the ipsilateral (compressed; see Figure 2D) root in the postcontrast images of the injured group.

The placement of ROI used for quantitative analysis is given on a representative acquisition in Figure 3A. Here the spinal cord with roots passing through the surrounding vertebrae at C7 is shown. The spinal level of interest was localized using the landmarks of soft tissue injury (introduced during the surgery) and anterior tubercles (present only at the C6 level). ROI were drawn for each dorsal root as well as at sites in the surrounding back muscle. If no nerve root was visible, the ROI was placed in the linearly inferred position between successive roots.

The flexibility of the rat neck in multiple directions meant that axial plane alignment of both ipsilateral and contralateral nerve roots was not always feasible, despite the use of a stereotactic restraint device. Therefore, to ensure that the signal loss at the injured root was a result of SPIO accumulation rather than from imaging artifacts, such as partial-volume effects, a series of sequential slices was acquired for each rat to include nerve roots through the C6/C7 levels. A representative series of such acquisitions is shown in Figure 3, B to F. These five adjacent slices at C6 from a C7-compressed rat show that there was no
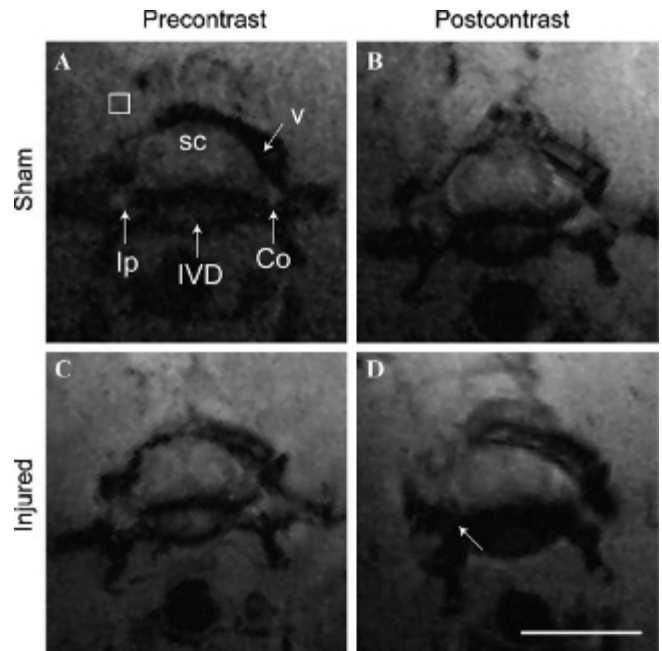

Figure 2. Imaging SPIO-induced hypointensity at the injury site. Representative magnetic resonance acquisitions of spinal cord and nerve root level C7 (C6 vertebral level). Use of a dual-coil arrangement afforded high-resolution imaging at tissue depths of several centimeters. The spinal cord (SC), vertebrae (V; especially the anterior tubercle), disk (IVD), nerve roots (ipsilateral [Ip] and contralateral [Co]), and wind pipe are clearly visible for each subject. Soft tissue filling of the void created on hemilaminectomy bone removal to expose the roots is evident (indicated below the *open square* in A). Both the ipsilateral and contralateral nerve roots are visible on the images for the sham animal, A and B, respectively. In contrast, the ipsilateral nerve root on the postcontrast image appears hypointense (indicated by the *arrow* in D) compared to the precontrast image (C). The scale bar is 0.5 cm in length and applies for all panels.

evidence of signal loss in the ipsilateral root at one level above the injury.

The normalized relative signal intensity (nrSI) computed for each imaging slice in the rostral-to-caudal direction of representative animals is shown in Figure 4. The periodic maxima reflect the appearance of the nerve roots, whereas the minima reflect the presence of bone. Qualitatively, it is evident that there is little discrepancy between the ipsilateral and contralateral nrSI in the precontrast series. An example of slight offset of roots, as described above, is seen in Figure 4B; here the bilateral C6 roots are in different imaging planes. The decrease in the nrSI at C7 in the postcontrast injured rat, resulting from SPIO accumulation, is substantial (see Figure 4D).

To quantitatively compare the sham and injured groups, pre- and postcontrast, the percentage difference between the contralateral and ipsilateral nrSI was calculated (see double-ended arrow, Figure 4D). These values
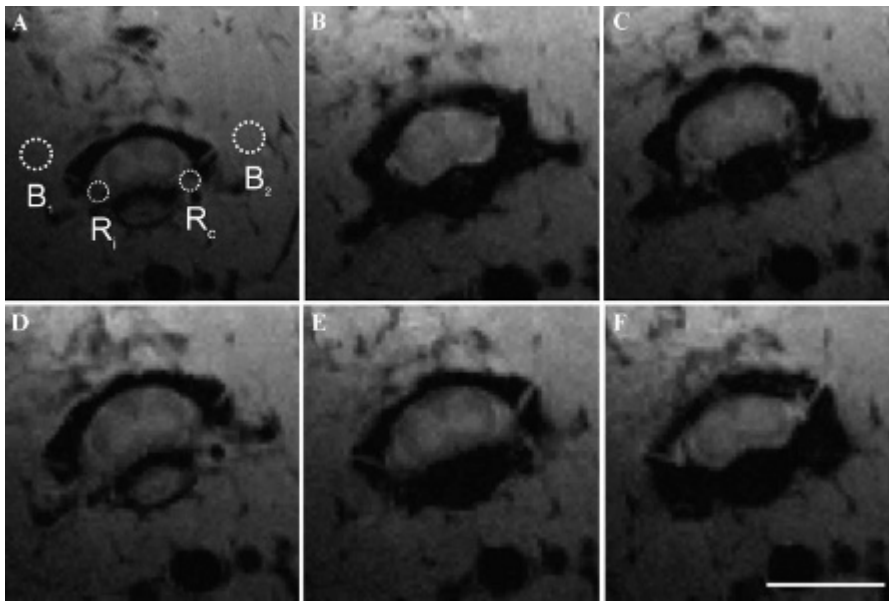
Figure 3. Sequential magnetic resonance imaging slices of nerve root. *A*, A representative axial image is presented, overlaid with ROI for the ipsilateral (R_i) and contralateral (R_c) roots as well as background paraspinal muscle (B_1 and B_2). The ROI have been slightly enlarged for clarification. Analyses investigated relative signal through a series of sequential acquisitions to avoid artifactual errors, such as partial-volume effects, from distorting the results. An example of five consecutive 0.5 mm slices through the C6 nerve roots (C5 vertebral level) is shown rostral to caudal in B to F. The scale bar is 0.5 cm in length and applies for all panels.

are plotted as percent change in Figure 5. SPIO accumulation over 24 hours led to local hypointensity and a difference in nrSI between the roots in the injured case of 72.9 ± 31%. No significant change in precontrast images of nrSI was detected between ipsilateral and contralateral nerve roots in the injured (5.35 ± 12.9%) or sham (−10.8 ± 5.4%) animals. Further, the sham group showed no significant nerve root enhancement (2.8 ± 14.1%) 24 hours after the SPIO injection.

Histologic evaluation of the nerve roots and spinal cord was performed to identify the presence or absence of activated macrophages and iron oxide particles. Representative micrographs of dorsal roots and spinal cord are shown in Figure 6. The detection of SPIO and macrophage by immunostaining was observed in the injured C7 root (see Figure 6, E and F). Very few inflammatory cells and little accumulated iron oxide were observed at the ipsilateral C6 root above the nerve root injury (see Figure 6, G and H). Generally, the iron oxide was colocalized with macrophages at the injury site. Inflammatory cells and accumulated SPIO were absent in the C7 roots of the sham animals and the contralateral root of the injured animals.

Discussion

MRI of the cervical spine provides high-resolution visualization of the spinal cord, nerve root, and skeletal architecture. However, the difficulty in using this information to identify the anatomic origin responsible for cervical radiculopathy or to correlate pathology with pain

symptoms is a significant challenge in clinical patient management.[16] Noninvasive markers for the detection of neuroinflammation have significant potential to impact clinical practice through detection and monitoring of therapy for cervical pain.

In animal pain models that use ligation,[48] compression,[49] or chemical irritation[50] of neural tissue, hypersensitivity of the affected enervated area is assessed through behavioral responses to mechanical and/or temperature stimuli. In the painful injury model investigated here, compression of the C7 nerve root induces sustained behavioral sensitivity that extends into the forepaw, mimicking the clinical presentation of persistent radicular pain.[25] This same mechanical loading of the nerve root also leads to macrophage infiltration at the root and release of inflammatory cytokines, further contributing to persistent behavioral hypersensitivity.[21] In our study, we used SPIO contrast agents for the noninvasive in vivo cellular detection of neuroinflammation.[19]

It was found that one day following the administration of SPIO, hypointense signal was observed at the injured site on a T_2*-weighted image. Inflammation, signified by either hyper- or hypointensity, was not detectable at injured roots prior to contrast enhancement (see Figure 2, A and B). Further, noncompressed roots demonstrated no significant change in signal ratio following contrast delivery. Confirmation that the decrease in signal at the injured site was due to the specific presence of SPIO was accomplished by colocalizing the iron from the particles to the activated macrophage surface marker CD68 in the nerve root (see Figure 6).
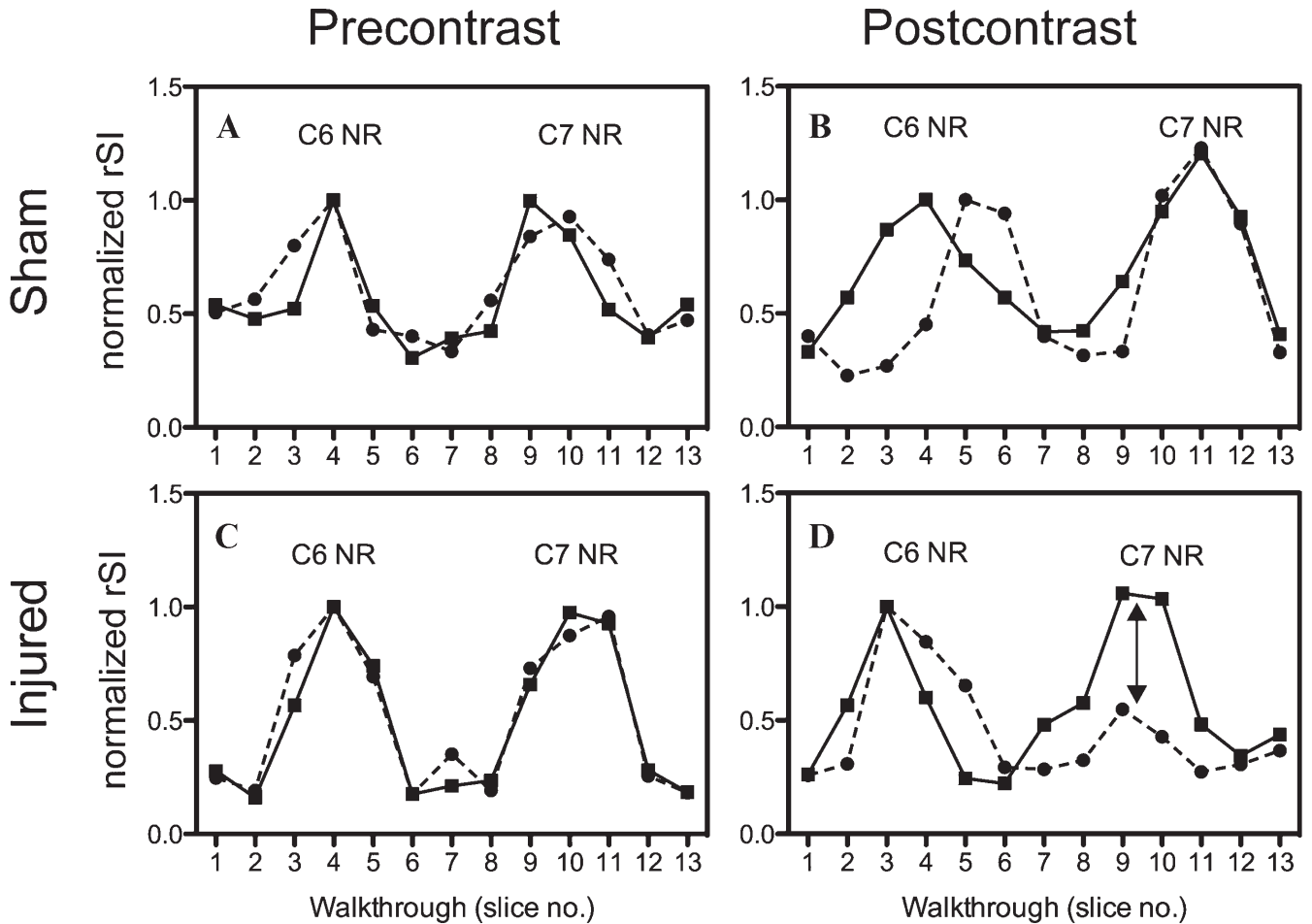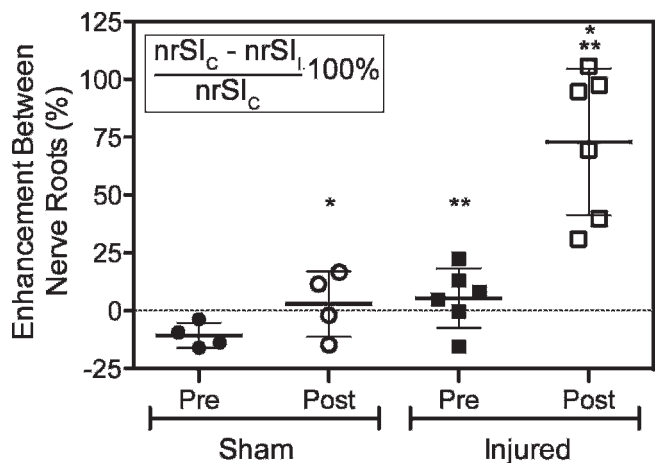
Figure 4. Normalized relative signal intensity of nerve roots (NRs). The relative signal intensity (rSI, relative to paraspinal muscle) in the ipsilateral (*dashed*) and contralateral (*solid*) NRs was normalized to the maxima rSI at the C6 level. Representative normalized relative signal intensity (nrSI) acquired from sequential magnetic resonance imaging slices (rostral to caudal) is shown for sham animals (A) precontrast and (B) postcontrast as well as injured animals (C) precontrast and (D) postcontrast. Periodic increases in signal were found to correlate with the appearance of roots. The signal minima correspond to bone and intervertebral tissue. Sham and precontrast injured subjects did not demonstrate discrepancy in nrSI. When investigating postcontrast injured animals, a large difference in the C7 nerve root nrSI was observed between the ipsilateral and contralateral roots, as indicated by the *double-ended arrow*.

Comparison of nrSI between the ipsilateral and contralateral roots of the injured group revealed a significant change (72.9 ± 31%) in the injured root after SPIO accumulation. No significant percentage difference of nrSI was determined outside the injured postcontrast group. Small quantities of iron oxide and macrophage were detected by histology at the ipsilateral C6 root of the rats in which the C7 root was compressed; however, this extent of SPIO accumulation was below the magnetic resonance detection limit. These results indicate that this technique is specific for detecting the site of injury, potentially providing a means to guide surgical interventions for treatment of radiculopathy patients. However, it should be noted that future use of the nrSI metric, which is dependent on C6 root signal intensity, requires that the

injury be localized to a single level. This shortcoming could be alleviated through the imaging of additional nerve roots. In the present study, MRI was limited to only two vertebrae for each rat owing to the flexibility and depth of the cervical spine, which is situated further from the back than the thoracic or lumbar spine. The surface coil was positioned with the C6 and C7 roots in the field of view to evaluate both a noninjured and a potentially injured level at the same time.

Previous work using SPIO-enhanced MRI of nerve injury reported hyperintensity at the injury site following compression, followed by darkening on contrast administration.[38] The hyperintense signal feature was not observed here and may have been masked by the bone surrounding the root or may be present only with the

Figure 5. SPIO-enhanced detection of nerve root compression. Quantification of the enhancement in the normalized relative signal intensity (nrSI) between the ipsilateral and contralateral nerve roots is shown. The mean enhancement in precontrast (*filled symbols*) and postcontrast images (*open*) is plotted along with the standard deviation for each group. Significant enhancement ($p < .01$) between the (**) pre- and postcontrast roots in the injured group as well as between the (*) sham and injured postcontrast nerve roots was found.

production of edema, which occurs for more severe insults, such as used in that model. A further difference between the two studies was that contrast enhancement

was possible only if SPIO were administered 1 day following injury, whereas the imaging studies here were not performed until 6 days after the initial injury. This conforms with earlier investigations of the model employed in this study, which have revealed that macrophage accretion continues for at least 7 days following transient injury.[25]

Although the work presented here needs to be validated at clinically relevant scanning strengths, it should be noted that many of the anatomic challenges and limitations presented by the rat are not present to the same extent in humans. Cervical vertebrae are well visualized and aligned in the supine position.[51] Furthermore, the much larger diameter of the roots in the human (approximately 0.5 cm) would enable greater distinction of bony versus neural tissues and identification of SPIO accumulation.

In conclusion, SPIO labeling in vivo, using an analogue of commercially available and clinically approved agents (for example, the 20–40 nm diameter ferumoxtran[52]), demonstrated cellular visualization of an otherwise occult painful neural injury. The injured nerve roots were readily identified 24 hours following the injection of contrast. Ratiometric assessment of nerve to
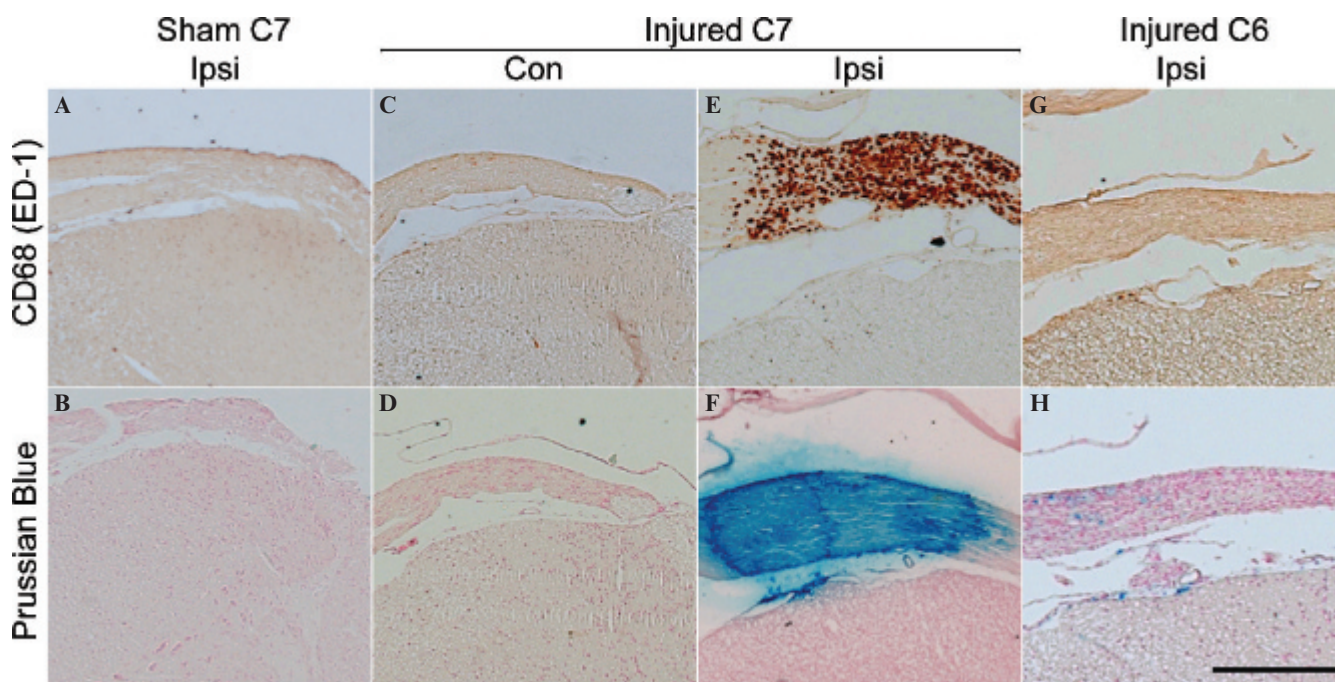
Figure 6. Histologic colocalization of SPIO and activated macrophage. Staining of dorsal nerve roots (NRs) was performed for both macrophage and iron following the final imaging time point. Representative ipsilateral (Ipsi) C7 NRs of sham animals were stained for macrophage and iron oxide (A and B, respectively). Neither immune cells nor SPIO nanoparticles were detected. This was also the case for the C7 NRs on the contralateral (Con) side of injured animals (C and D). Activated macrophage staining (E) and corresponding iron (F) were evident on the transiently injured NR (ipsilateral side of C7). Finally, limited inflammatory cell infiltration and corresponding iron oxide were found in the C6 ipsilateral NR of the injured subjects (G and H). The scale bar in H (equivalent to 100 μm) applies for all images.

background tissue specified a significant difference in the normalized signal intensity ratio following administration of SPIO. Future studies will seek to use SPIO-enhanced MRI to monitor treatment efficacy and study the ''root'' causes of radicular pain. It is expected that cellular MRI of the site of injury will allow for personalized, quantitative, and real-time monitoring of antiinflammatory treatment strategies aimed at alleviating radicular pain.

Acknowledgments

References

1. Slipman CW, Plastaras CT, Palmitier RA, et al. Symptom provocation of fluoroscopically guided cervical nerve root stimulation: are dynatomal maps identical to dermatomal maps? Spine 1998;23:2235–42.

2. Harden N, Cohen M. Unmet needs in the management of neuropathic pain. J Pain Symptom Manage 2003;25 Suppl 5:S12–7.

3. Radhakrishnan K, Litchy WJ, O'Fallon WM, Kurland LT. Epidemiology of cervical radiculopathy. A population-based study from Rochester, Minnesota, 1976 through 1990. Brain 1994;117 (Pt 2):325–35.

4. Waters TR. National efforts to identify research issues related to prevention of work-related musculoskeletal disorders. J Electromyogr Kinesiol 2004;14:7–12.

5. Rempel DM, Harrison RJ, Barnhart S. Work-related cumulative trauma disorders of the upper extremity. JAMA 1992;267:838–42.

6. Cote P, Cassidy JD, Carroll LJ, Kristman V. The annual incidence and course of neck pain in the general population: a population-based cohort study. Pain 2004;112:267–73.

7. Cote P, Cassidy JD, Carroll L. The Saskatchewan Health and Back Pain Survey. The prevalence of neck pain and related disability in Saskatchewan adults. Spine 1998;23:1689–98.

8. Rothman SM, Winkelstein BA. Chemical and mechanical nerve root insults induce differential behavioral sensitivity and glial activation that are enhanced in combination. Brain Res 2007;1181:30–43.

9. Kelly JDT, Aliquo D, Sitler MR, et al. Association of burners with cervical canal and foraminal stenosis. Am J Sports Med 2000;28:214–7.

10. Nuckley DJ, Konodi MA, Raynak GC, et al. Neural space integrity of the lower cervical spine: effect of normal range of motion. Spine 2002;27:587–95.

11. Hollingworth W, Dixon AK, Todd CJ, et al. Self reported health status and magnetic resonance imaging findings in patients with low back pain. Eur Spine J 1998;7:369–75.

12. Lin Y-W, Cheng C-M, LeDuc PR, Chen C-C. Understanding sensory nerve mechanotransduction through localized elastomeric matrix control. PLoS ONE 2009;4:e4293.

13. Lehto IJ, Tertti MO, Komu ME, et al. Age-related MRI changes at 0.1 T in cervical discs in asymptomatic subjects. Neuroradiology 1994;36:49–53.

14. Matsumoto M, Fujimura Y, Suzuki N, et al. MRI of cervical intervertebral discs in asymptomatic subjects. J Bone Joint Surg Br 1998;80:19–24.

15. Schellhas KP, Smith MD, Gundry CR, Pollei SR. Cervical discogenic pain. Prospective correlation of magnetic resonance imaging and discography in asymptomatic subjects and pain sufferers. Spine 1996;21:300–11; discussion 11–2.

16. Carette S, Fehlings MG. Clinical practice. Cervical radiculopathy. N Engl J Med 2005;353:392–9.

17. Winkelstein BA, Rutkowski MD, Sweitzer SM, et al. Nerve injury proximal or distal to the DRG induces similar spinal glial activation and selective cytokine expression but differential behavioral responses to pharmacologic treatment. J Comp Neurol 2001;439:127–39.

18. Hubbard RD, Winkelstein BA. Transient cervical nerve root compression in the rat induces bilateral forepaw allodynia and spinal glial activation: mechanical factors in painful neck injuries. Spine 2005;30:1924–32.

19. Rothman SM, Huang Z, Lee KE, et al. Cytokine mRNA expression in painful radiculopathy. J Pain 2009;10:90–9.

20. Hubbard RD, Martinez JJ, Burdick JA, Winkelstein BA. Controlled release of GDNF reduces nerve root-mediated behavioral hypersensitivity. J Orthop Res 2009;27:120–7.

21. Obata K, Yamanaka H, Fukuoka T, et al. Contribution of injured and uninjured dorsal root ganglion neurons to pain behavior and the changes in gene expression following chronic constriction injury of the sciatic nerve in rats. Pain 2003;101:65–77.

22. Raymond D, Hubbard JJ, Martinez JA, et al. Controlled release of GDNF reduces nerve root-mediated behavioral hypersensitivity. J Orthop Res 2009;27:120–7.

23. Abbadie C, Lindia JA, Cumiskey AM, et al. Impaired neuropathic pain responses in mice lacking the chemokine receptor CCR2. Proc Natl Acad Sci U S A 2003;100:7947–52.

24. Myers RR, Heckman HM, Rodriguez M. Reduced hyperalgesia in nerve-injured WLD mice: relationship to nerve fiber phagocytosis, axonal degeneration, and regeneration in normal mice. Exp Neurol 1996;141:94–101.

25. Hubbard RD, Winkelstein BA. Dorsal root compression produces myelinated axonal degeneration near the biomechanical thresholds for mechanical behavioral hypersensitivity. Exp Neurol 2008;212:482–9.

26. Lee JS, Kang HJ, Gong G, et al. MR imaging of in vivo recruitment of iron oxide-labeled macrophages in experimentally induced soft-tissue infection in mice. Radiology 2006;241:142–8.

27. Kaim AH, Wischer T, O'Reilly T, et al. MR imaging with ultrasmall superparamagnetic iron oxide particles in experimental soft-tissue infections in rats. Radiology 2002;225:808–14.

28. Lutz AM, Weishaupt D, Persohn E, et al. Imaging of macrophages in soft-tissue infection in rats: relationship between ultrasmall superparamagnetic iron oxide dose and MR signal characteristics. Radiology 2005;234:765–75.

29. Beckmann N, Cannet C, Zurbruegg S, et al. Macrophage infiltration detected at MR imaging in rat kidney allografts: early marker of chronic rejection? Radiology 2006;240:717–24.

30. Sigovan M, Boussel L, Sulaiman A, et al. Rapid-clearance iron nanoparticles for inflammation imaging of atherosclerotic plaque: initial experience in animal model. Radiology 2009; 252:401–9.

31. Schmitz SA, Taupitz M, Wagner S, et al. Iron-oxide-enhanced magnetic resonance imaging of atherosclerotic plaques: postmortem analysis of accuracy, inter-observer agreement, and pitfalls. Invest Radiol 2002;37:405–11.

32. Litovsky S, Madjid M, Zarrabi A, et al. Superparamagnetic iron oxide-based method for quantifying recruitment of monocytes to mouse atherosclerotic lesions in vivo: enhancement by tissue necrosis factor-α, interleukin-1β, and interferon-γ. Circulation 2003;107:1545–9.

33. Thorek DL, Chen AK, Czupryna J, Tsourkas A. Superparamagnetic iron oxide nanoparticle probes for molecular imaging. Ann Biomed Eng 2006;34:23–38.

34. Bulte JWM, Ben-Hur T, Miller BR, et al. MR microscopy of magnetically labeled neurospheres transplanted into the Lewis EAE rat brain. Magn Reson Med 2003;50:201–5.

35. Dousset V, Delalande C, Ballarino L, et al. In vivo macrophage activity imaging in the central nervous system detected by magnetic resonance. Magn Reson Med 1999;41:329–33.

36. Oweida AJ, Dunn EA, Foster PJ. Cellular imaging at 1.5 T: detecting cells in neuroinflammation using active labeling with superparamagnetic iron oxide. Mol Imaging 2004;3:85–95.

37. Linker RA, Kroner A, Horn T, et al. Iron particle-enhanced visualization of inflammatory central nervous system lesions by high resolution: preliminary data in an animal model. AJNR Am J Neuroradiol 2006;27:1225–9.

38. Bendszus M, Stoll G. Caught in the act: in vivo mapping of macrophage infiltration in nerve injury by magnetic resonance imaging. J Neurosci 2003;23:10892–6.

39. Stoll G, Wesemeier C, Gold R, et al. In vivo monitoring of macrophage infiltration in experimental autoimmune neuritis by magnetic resonance imaging. J Neuroimmunol 2004;149:142–6.

40. Sykova E, Jendelova P. Magnetic resonance tracking of transplanted stem cells in rat brain and spinal cord. Neurodegener Dis 2006;3:62–7.

41. Dunn EA, Weaver LC, Dekaban GA, Foster PJ. Cellular imaging of inflammation after experimental spinal cord injury. Mol Imaging 2005;4:53–62.

42. Zimmermann M. Ethical guidelines for investigations of experimental pain in conscious animals. Pain 1983;16:109–10.

43. Thorek DLJ, Tsourkas A. Size, charge and concentration dependent uptake of iron oxide particles by non-phagocytic cells. Biomaterials 2008;29:3583–90.

44. Kobayashi S, Yoshizawa H, Yamada S. Pathology of lumbar nerve root compression. Part 2: morphological and immunohistochemical changes of dorsal root ganglion. J Orthop Res 2004;22:180–8.

45. Kobayashi S, Yoshizawa H. Effect of mechanical compression on the vascular permeability of the dorsal root ganglion. J Orthop Res 2002;20:730–9.

46. Kirita T, Takebayashi T, Mizuno S, et al. Electrophysiologic changes in dorsal root ganglion neurons and behavioral changes in a lumbar radiculopathy model. Spine 2007;32:E65–72.

47. Colburn RW, Rickman AJ, DeLeo JA. The effect of site and type of nerve injury on spinal glial activation and neuropathic pain behavior. Exp Neurol 1999;157:289–304.

48. Winkelstein BA, Rutkowski MD, Weinstein JN, DeLeo JA. Quantification of neural tissue injury in a rat radiculopathy model: comparison of local deformation, behavioral outcomes, and spinal cytokine mRNA for two surgeons. J Neurosci Methods 2001;111:49–57.

49. Hubbard RD, Chen Z, Winkelstein BA. Transient cervical nerve root compression modulates pain: load thresholds for allodynia and sustained changes in spinal neuropeptide expression. J Biomech 2008;41:677–85.

50. Hashizume H, DeLeo JA, Colburn RW, Weinstein JN. Spinal glial activation and cytokine expression after lumbar root injury in the rat. Spine 2000;25:1206–17.

51. Modic M, Weinstein M, Pavlicek W, et al. Magnetic resonance imaging of the cervical spine: technical and clinical observations. AJR Am J Roentgenol 1983;141:1129–36.

52. Leung K. Molecular Imaging and Contrast Agent Database (MICAD) [database online]. Bethesda (MD): National Library of Medicine, National Center for Biotechnology Information; 2004–2009. Available at: http://micad.nih.gov (accessed 2007).